A Cartesian cut cell based two–way strong fluid–solid coupling algorithm for 2D floating bodies

Qiang Chen[a,*], Jun Zang[a], Aggelos S. Dimakopoulos[b], David M. Kelly[c], Chris J. K. Williams[d]

[a] *Research Unit for Water, Environment and Infrastructure Resilience (WEIR), Department of Architecture and Civil Engineering, University of Bath, BA2 7AY, U.K.*
[b] *HR Wallingford, Wallingford, Oxon, OX10 8BA, U.K.*
[c] *Coastal Research Lab., International Hurricane Research Center, Florida International University, Miami, Florida, 33199, U.S.A*
[d] *Department of Architecture and Civil Engineering, University of Bath, BA2 7AY, U.K.*

Abstract

In a recent paper Kelly et al. (2015) [PICIN: A Particle–In–Cell solver for incompressible free surface flows with two–way fluid–solid coupling. SIAM Journal on Scientific Computing 37 (3), B403–B424.] detailed the PICIN full particle Particle–In–Cell (PIC) solver for incompressible free–surface flows. The model described in that paper employed a tailored version of the Distributed Lagrange Multiplier (DLM) method for the strong coupling of fluid–solid interaction. In this paper we propose an alternative strong fluid–solid coupling algorithm based on a modification to the cut cell methodology that is informed by the variational approach. The solid velocity flux/integral on the boundary is expressed purely in terms of pressure leading to a revised pressure Poisson equation that is discretised in a finite volume sense. This approach allows the PICIN model to simulate the motion of floating bodies of arbitrary configuration. 2D test cases involving floating bodies with one or more degrees of freedom (DoF) are used to validate the modified PICIN model. The results presented show that the modified PICIN model is able to both efficiently and robustly predict the motions of surface–piercing floating structures under either regular or extreme wave action.

Keywords: Computational Fluid Dynamics, Navier Stokes pressure projection, Particle–In–Cell, Cut Cell, Two–Way Fluid Structure Interaction, Floating Bodies

1. Introduction

In the past few decades wave structure interaction including, amongst other things, wave generation and absorption, wave slamming, green water overtopping and floating structures has been widely

*Corresponding author. Tel.: +44 01225 384885
Email address: Q.Chen@bath.ac.uk (Qiang Chen)

studied both experimentally and numerically within the coastal and offshore engineering community (Faltinsen et al., 2004; Chen et al., 2014b; Gao and Zang, 2014; Oliveira et al., 2012; Zhao and Hu, 2012). In particular, floating structures as well as their response under wave actions are of great interest (Koo and Kim, 2004; Hadžić et al., 2005; Zhao and Hu, 2012; Bouscasse et al., 2013; Weller et al., 2013; Zhao et al., 2014). This paper focuses on developing a strong coupling algorithm for the investigation of two–way fluid–solid interactions with an emphasis on floating bodies. This algorithm involves two major issues: a Cartesian cut cell based technique for solid boundary representation and a strong coupling scheme for two–way fluid–solid interactions. Both issues are introduced, followed by a brief description of the full particle PIC based numerical model PICIN (Kelly et al., 2015), which is employed as a framework for the proposed strong fluid–solid coupling approach in this paper.

Numerically, various models have been proposed for representing solid boundaries and simulating fluid–solid interactions. Focusing on Eulerian methods we highlight the immersed boundary (IB) technique (Peskin, 1972, 2002), which transfers solid boundary effect to a force field on the fluid grid. However, this approach may cause the fluid to permeate structures as mentioned in Batty et al. (2007). Glowinski et al. (1999) and Patankar (2001) proposed the Distributed Lagrange Multiplier (DLM) method for particulate flows. This approach is straightforward to implement and has previously been extended for use in the PICIN model. Nevertheless, the DLM method may have limitations in simulating surface–piercing floating bodies within the current PICIN model as discussed below. Batty et al. (2007) introduced the variational framework for the solution of pressure in fluid flow for fluid–solid interactions, and demonstrated that this method can be easily coupled with freely moving solids of arbitrary geometry. However, Ng et al. (2009) argue that the variational approach is not convergent in the L^{∞} norm for problems involving fixed structures and thus not suitable for computations where velocity field around objects is important; instead, they proposed a novel and more accurate Cartesian cut cell method for simulating fluid interacting with fixed and motion prescribed solids. The so–called Cartesian cut cell approach has been widely used as an alternative approach to unstructured grids for structures with complex body shapes (Noh, 1963; Purvis and Burkhalter, 1979; Quirk, 1994; Ye et al., 1999); it offers great advantages when moving boundaries are employed since there is no need to re–mesh the computational grid (Yang et al., 2000; Qian et al., 2006; Ng et al., 2009). In the context of inviscid compressible flow Noh (1963) first suggested combining the idea of a cut cell fraction with an application of the finite volume method to treat (deformable) solid boundaries. A similar approach was also proposed by Purvis and Burkhalter (1979) to solve the equations of transonic potential flow. This

procedure was then further investigated by Ng et al. (2009) with regard to the order of convergence and accuracy; results from Ng et al. (2009) show a second–order accuracy in both the L^1 and L^∞ norms in 2D. In this paper, we follow the cut cell approach of Ng et al. (2009) for its high accuracy in resolving fluid–solid interactions and simplicity in handling moving boundaries. We show that it is straightforward to implement this approach in PICIN and it is convergent in the L^2 norm in 2D when the grid is sufficiently fine. The detailed description of this cut cell approach is given in Section 2.

In a coupled fluid–solid system, when the influence from one aspect to another becomes negligible, a one–way coupling will work well, e.g. the simulation of a piston type wavemaker (Chen et al., Unpublished results). In most cases, however, both the solid and the fluid phase interact with each other and two–way fluid–solid coupling is required, e.g. Hadžić et al. (2005); Batty et al. (2007); Zhao et al. (2014); Kelly et al. (2015). Among those schemes, when solid structures are only used to provide velocity boundaries for the solution in the fluid domain and the fluid is solely employed to give a pressure boundary for solid computations, they are usually termed as weak coupling (e.g. Hadžić et al. (2005); Zhao et al. (2014)). In this sense, strong coupling is defined to mean that the effects of fluid and solid boundaries are treated simultaneously. Typical examples of strong coupling schemes can be found in Patankar et al. (2000); Batty et al. (2007); Kelly et al. (2015). The PICIN model is currently only suitable for incompressible fluids. Within this framework, we found that when implementing a weak coupling scheme, especially for studies of wave and floating structure interactions, the behaviour of pressure in the fluid domain can be very stiff which causes instabilities in both fluid and solid motion calculations. The main reason for this is that the fluid pressure is used not only to update the solid domain but also to maintain the flow incompressibility in the PICIN solver; therefore, an inaccurate value for the velocity change on the solid boundaries will cause large pressure fluctuations inside the fluid phase which in turn exerts an incorrect force on the structure and can ultimately cause the numerical model to fail. This type of stiff pressure behaviour in algorithms for incompressible flow has been discussed previously by Fedkiw (2002). Although this unstable pressure behaviour can be potentially alleviated by iterating the solver to a convergent state (e.g. Hadžić et al. (2005); Borazjani et al. (2008)), the CPU cost is, in many cases, prohibitively expensive. Thus, strong fluid–solid coupling schemes are the preferred approach to be adopted in the PICIN model. The model previously used a modified version of the DLM method of Patankar et al. (2000) for fluid–solid interactions. The solids are treated exactly as fluids at first and then a velocity correction within the solid phase is made due to the density differences and a rigidity constraint. This method is efficient and has been applied for

coastal flows in a previous study (Chen et al., Unpublished results). However, since in this approach the solids are treated as fluids in the initial stages, the surface–piercing portion of a rigid floating body needs to be treated as the free surface of the fluid. It is necessary, and non–trivial, to consistently apply the boundary conditions, especially in the presence of angled corners such as floating boxes. The DLM approach thus requires further validation and improvements within the PICIN model when it is to be used for simulating surface–piercing floating structures for engineering applications. Instead, in this paper, we focus on the strong coupling approach presented by Batty et al. (2007), where the fluid pressure in cells immediately surrounding the solid body are connected together and implicitly solved within a variational framework. Here we combine this implicit approach to the fluid solid motion with the cut cell based solid boundary representation of Ng et al. (2009) instead, within the PICIN model framework. We show that this new approach enables our model to simulate floating body cases in a stable and efficient manner.

The PICIN model is a full particle Particle–In–Cell solver (Brackbill and Ruppel, 1986; Zhu and Bridson, 2005; Kelly, 2012) for incompressible free–surface flows and is especially designed for coastal and offshore engineering applications. As a hybrid Eulerian–Lagrangian approach, the PICIN model has both the flexibility of a Lagrangian approach in terms of simulating complex free–surface flow and the efficiency of an Eulerian approach. The model adopts the pressure projection technique first proposed by Chorin (1968) for the solution of incompressible Newtonian Navier–Stokes equations. Two major steps are implemented within this model: the Eulerian step and the Lagrangian step. In the Eulerian step the governing equations are first resolved on the uniform grid by ignoring the advection term which is then solved in a novel way during the Lagrangian step using the particles initially seeded in cells. The particles are also employed to detect the free surface where the boundary condition is enforced by a second–order accurate technique. In addition, information transfer between the particles and grids are conducted using interpolations or smoothed particle hydrodynamics (SPH)–like kernel functions. In this paper, an alternative new fluid and structure interaction scheme is developed and validated through the modelling of cases involving surface–piercing floating bodies.

The paper is organised as follows: Section 2 gives an overview of the modified PICIN model including the governing equations and major numerical schemes. In particular, Section 2.4 outlines the numerical solution technique of the proposed strong fluid–solid coupling scheme; Section 3 summarises the implementation of a piston–type wavemaker for either regular wave or focused wave generation and the relaxation zone approach for wave absorption in the PICIN model; In Section 4 we compare results

of the modified PICIN model with three test cases involving surface–piercing floating body motions; Finally, conclusions are drawn in Section 5.

2. The Modified PICIN Model

2.1. Governing equations

The model adopts a standard pressure projection method following Chorin (1968) to solve the incompressible Newtonian Navier–Stokes equations:

$$\nabla \cdot \boldsymbol{u} \;=\; 0, \tag{1}$$

$$\frac{\partial \boldsymbol{u}}{\partial t} + (\boldsymbol{u} \cdot \nabla)\boldsymbol{u} = \boldsymbol{f} - \frac{1}{\rho}\nabla p + \nu \nabla^2 \boldsymbol{u}, \tag{2}$$

where, in two spatial dimensions, $\boldsymbol{u} = [u, w]^T$ is the velocity field, t is time, p is pressure, $\boldsymbol{f} = [0.0, -9.81]^T$ represents the body force due to gravity, ρ is the liquid density, and ν is the kinematic viscosity of the fluid. During the Eulerian step the governing equations are resolved ignoring the advection term of the momentum equation, which is handled using particles during the Lagrangian step. This is both more computationally efficient and straightforward than an Eulerian advection step. We note that in this paper the governing equations are solved for a single phase flow where the fluid region is indicated by particles. Following Harlow and Welch (1965), we use a staggered grid where pressures are stored at cell centres and velocities are computed at relevant cell faces. Four particles are initially seeded in each cell and cells occupied by particles are marked as fluid cells while air cells correspondingly have no particles inside.

2.2. Eulerian step

Following the pressure projection method (Chorin, 1968) a tentative velocity $\tilde{\boldsymbol{u}}$ is first given by applying the body force and physical dissipation as an Euler step in time:

$$\frac{\tilde{\boldsymbol{u}} - \boldsymbol{u}^n}{\Delta t} = \nu \nabla^2 \tilde{\boldsymbol{u}} + \boldsymbol{f}, \tag{3}$$

where $\boldsymbol{u}_n$ is the velocity at t_n. While the body force is computed explicitly, the viscosity term is treated implicitly and we use the bi–conjugate gradient (BCG) method (Press et al., 1992) for solving the linear equation system constructed by applying Eq. 3 in the fluid region. The next step is then to

find a pressure p^{n+1} to maintain the incompressibility condition Eq. 1. Recalling the remaining part of the momentum equation, we have

$$\frac{(\boldsymbol{u}^{n+1} - \tilde{\boldsymbol{u}})}{\Delta t} = -\rho^{-1}\nabla p^{n+1}. \tag{4}$$

By taking the divergence of both sides of Eq. 4 and applying $\nabla\cdot\boldsymbol{u}^{n+1} = 0$, a pressure Poisson equation can be obtained:

$$\Delta t\rho^{-1}\nabla^2 p^{n+1} = \nabla\cdot\tilde{\boldsymbol{u}}\,. \tag{5}$$

During the solution of this pressure Poisson equation, the following boundary conditions on the free surface and moving solid boundaries are resolved respectively:

$$\boldsymbol{u} = \boldsymbol{u}_i \text{ and } p = 0 \quad \text{on } \zeta(\boldsymbol{x}, t), \tag{6}$$

where $\zeta = \zeta(\boldsymbol{x}, t)$ is the free surface and:

$$\boldsymbol{u} = \boldsymbol{u}_i \text{ and } \boldsymbol{n}\cdot(\Delta t\rho^{-1}\nabla p) = \boldsymbol{n}\cdot(\tilde{\boldsymbol{u}} - \boldsymbol{u}^{n+1}) \quad \text{on } \partial\Omega_S(\boldsymbol{x}, t), \tag{7}$$

where Ω_S and $\partial\Omega_S$ represent the solid domain and solid boundary, respectively. It is noted here that the zero pressure boundary condition is imposed on the free surface defined by the particle positions using a second–order accurate technique proposed in Gibou et al. (2002); details on the implementation of this approach within the PIC framework can be found in Kelly et al. (2015). The solid boundary condition is no–slip and will be implicitly computed within the discretisation of pressure Poisson equation detailed in Section 2.4.1.

After solving the pressure Poisson equation, the pressure field p^{n+1} is found and the next step is to project the tentative velocity onto a divergence–free velocity field using the pressure as a Lagrange multiplier:

$$\boldsymbol{u}^{n+1} = \tilde{\boldsymbol{u}} - \Delta t\rho^{-1}\nabla p^{n+1}. \tag{8}$$

2.3. Lagrangian step

Once a divergence–free velocity field on the grid is found, the velocity or velocity change will be interpolated onto the particles to update the velocity that each particle carries. The updated particle velocity is denoted as U_F only if the velocity change on the grid is used to increment the particle

velocity, which follows the full particle PIC approach that is used in the FLIP code of (Brackbill and Ruppel, 1986), and it is represented by U_C if grid velocity is directly transferred onto the particles using the classic PIC scheme of Harlow (1964). Note that while the classic PIC suffers from a large numerical dissipation due to the velocity transfer at each time step, Brackbill and Ruppel (1986) claimed that their full particle PIC scheme achieves almost no numerical diffusion. However, this full particle PIC scheme may suffer from noisy behaviour due to the absence of viscosity (Ando et al., 2012). Following Zhu and Bridson (2005) and Ando et al. (2012), we use a weighted average of the two schemes for the final particle velocity:

$$u = cU_F + (1 - c)U_C, \tag{9}$$

where c is an empirical weighting coefficient and is set to 0.96 in this paper. In practice when this coefficient is close to, but less than, unity, the change of this coefficient was found to have negligible influence.

The particles carrying the newly updated velocity field are then advected through the grid velocity field using the third–order accurate Runge Kutta scheme of Ralston (1962). Once the particles are advected, the velocity is transferred back onto the grid for the next time step calculation. In the current model, while the velocity is interpolated from the grid to the particles using the fourth–order accurate weighted essentially non-oscillatory (WENO) scheme proposed by Edwards and Bridson (2012), it is transferred back to the grid via an SPH–like cubic spline kernel function (Monaghan and Lattanzio, 1985). We note that the fourth–order WENO scheme helps to reduce the numerical dissipation due to truncation error from the spatial discretisation. The overall accuracy of our numerical scheme cannot, however, be expected to be formally high-order. This is due to the errors that arise from other numerical approximations; for instance, the discretisation of Poisson equation is second–order accurate in space.

2.4. Numerical Solution Procedure

The strong fluid–solid coupling scheme and free–surface tracking approach are discussed in the following sections. For other numerical techniques used in the model such as velocity extrapolation from fluid cells to air cells (for particle advection), particle position redistribution (for high accuracy) and time step control (for numerical stability), the reader is referred to Kelly et al. (2015).

2.4.1. Strong fluid–structure coupling

In weak fluid–solid coupling schemes, once the fluid pressure field is resolved, an integration of fluid pressure on the solid boundary is usually carried out to calculate the fluid forces on the structures and move them according to Newton's second law of motion (e.g. Zhao et al. (2014)). When implementing the weak coupling scheme in PICIN, it is found that the motion of free moving structures can become unstable leading to a blow–up of the code. The main reason is that as the incompressible flows are solved using the pressure projection method, a small error in predicting the velocity of the moving body will cause a significant pressure change which in turn leads to an incorrect body motion and vice versa. Instead of iterating the whole scheme to improve the stability (e.g. Hadžić et al. (2005)), in this paper an efficient strong coupling algorithm is proposed and it is described below.

The strong coupling algorithm detailed here is based on the cut–cell type approach discussed in Ng et al. (2009). Following Ng et al. (2009), the discretisation of the Poisson equation (Eq. 5) on an irregular domain is conducted as follows. Fig. 1 shows the staggered computational grid used in the numerical model. The solid boundary is represented by a polyline with equal segment length, Δl. Let Ω_F be the fluid domain and G_{ij} represents the cell $(i-1/2, i+1/2)\times(j-1/2, j+1/2)$. By applying the finite volume approach to Eq. 5 and evoking the divergence theorem, we have

$$\Delta t \rho^{-1} \int_{\partial(G_{ij}\cap\Omega_F)} \boldsymbol{n}\cdot\nabla p^{n+1}\, dA = \int_{\partial(G_{ij}\cap\Omega_F)} \boldsymbol{n}\cdot\tilde{\boldsymbol{u}}\, dl, \tag{10}$$

where dl and dA denote the length and area differential respectively; $\boldsymbol{n}$ is the unit normal vector pointing out of the solid. Rewriting the boundary integral on both cell edges and solid faces of Eq. 10 into the approximate form we have

$$\begin{aligned}\int_{\partial(G_{ij}\cap\Omega_F)} \boldsymbol{n}\cdot\nabla p^{n+1}\, dA \simeq S_{i-\frac{1}{2},j}\cdot\frac{(p^{n+1}_{i-1,j}-p^{n+1}_{i,j})}{\Delta x} + S_{i+\frac{1}{2},j}\cdot\frac{(p^{n+1}_{i+1,j}-p^{n+1}_{i,j})}{\Delta x} + \\ S_{i,j-\frac{1}{2}}\cdot\frac{(p^{n+1}_{i,j-1}-p^{n+1}_{i,j})}{\Delta z} + S_{i,j+\frac{1}{2}}\cdot\frac{(p^{n+1}_{i,j+1}-p^{n+1}_{i,j})}{\Delta z} - \int_{G_{ij}\cap\partial\Omega_S} \boldsymbol{n}\cdot\nabla p^{n+1}\, dA\end{aligned} \tag{11}$$

and likewise

$$\int_{\partial(G_{ij}\cap\Omega_F)} \boldsymbol{n}\cdot\tilde{\boldsymbol{u}}\, dl \simeq S_{i+\frac{1}{2},j}\cdot\tilde{u}_{i+\frac{1}{2},j} - S_{i-\frac{1}{2},j}\cdot\tilde{u}_{i-\frac{1}{2},j} + S_{i,j+\frac{1}{2}}\cdot\tilde{w}_{i,j+\frac{1}{2}} - S_{i,j-\frac{1}{2}}\cdot\tilde{w}_{i,j-\frac{1}{2}} - \int_{G_{ij}\bigcap\partial\Omega_S} \boldsymbol{n}\cdot\tilde{\boldsymbol{u}}_{\text{solid}}\, dl, \tag{12}$$

where S is the cell fraction that is open to water, i.e. not occupied by solid; S in PICIN is computed through a Signed Distance Field (SDF) constructed on cell vertices (the detail implementation can be found in Kelly et al. (2015)). Recalling the solid boundary condition (Eq. 7) gives

$$\int_{G_{ij}\cap\partial\Omega_S} \boldsymbol{n}\cdot\nabla p^{n+1}\,dA = \frac{\rho}{\Delta t}\int_{C_{ij}\bigcap\partial\Omega_S} \boldsymbol{n}\cdot(\tilde{\boldsymbol{u}}_{\text{solid}} - \boldsymbol{u}^{n+1}_{\text{solid}})\,dl, \tag{13}$$

substituting Eq. 11–Eq. 13 all into Eq. 10 and rewriting the equation, we finally obtain:

$$\begin{aligned} &S_{i-\frac{1}{2},j}\cdot\frac{\Delta t(p^{n+1}_{i-1,j}-p^{n+1}_{i,j})}{\rho\Delta x}+S_{i+\frac{1}{2},j}\cdot\frac{\Delta t(p^{n+1}_{i+1,j}-p^{n+1}_{i,j})}{\rho\Delta x}+S_{i,j-\frac{1}{2}}\cdot\frac{\Delta t(p^{n+1}_{i,j-1}-p^{n+1}_{i,j})}{\rho\Delta z}+S_{i,j+\frac{1}{2}}\cdot\frac{\Delta t(p^{n+1}_{i,j+1}-p^{n+1}_{i,j})}{\rho\Delta z}\\ &= S_{i+\frac{1}{2},j}\cdot\tilde{u}_{i+\frac{1}{2},j} - S_{i-\frac{1}{2},j}\cdot\tilde{u}_{i-\frac{1}{2},j} + S_{i,j+\frac{1}{2}}\cdot\tilde{w}_{i,j+\frac{1}{2}} - S_{i,j-\frac{1}{2}}\cdot\tilde{w}_{i,j-\frac{1}{2}} - \int_{G_{ij}\bigcap\partial\Omega_S}\boldsymbol{n}\cdot\boldsymbol{u}^{n+1}_{\text{solid}}\,dl. \end{aligned} \tag{14}$$

The above equations provide a symmetric positive definite linear system for pressure computation, which is solved by the BCG method in the PICIN model. It is also noted that this cut–cell type approach has been shown to be second–order accurate in both the L^1 and L^∞ norms in 2D by Ng et al. (2009).

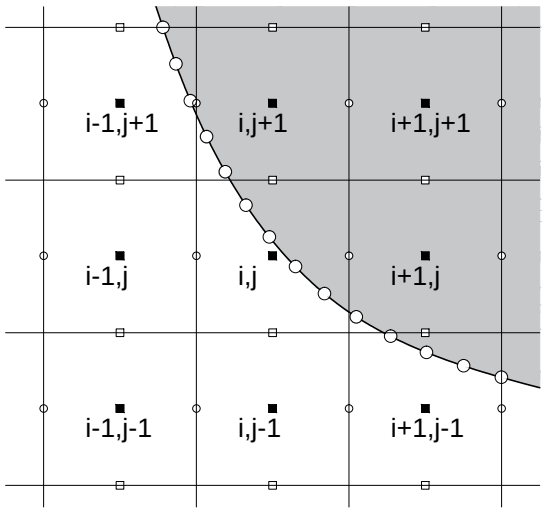

Fig. 1: Staggered computational grid where pressure is stored at cell centres (black square) and x and z velocity components are computed on vertical (white circle) and horizontal (white square) cell edges, respectively. The shaded area represents the solid phase; the boundary has been discretised into small line segments.

Following Kelly et al. (2015) and Chen et al. (Unpublished results), Eq. 14 in this paper is implemented for fixed solids or solids with prescribed motions for which $\boldsymbol{u}^{n+1}_{\text{solid}}$ is known. Calculations involving free moving objects are more complicated and we re–interpret the technique proposed by Batty et al. (2007) to implicitly calculate solid velocity using a J operator that maps the pressure to

net forces and torques on the body:

$$\boldsymbol{U}^{n+1} = \boldsymbol{U}^{n} + \Delta t M_s^{-1} J p^{n+1} + \Delta t \boldsymbol{f}, \tag{15}$$

where $\boldsymbol{U}^{n+1}$ and $\boldsymbol{U}^{n}$ are the solid velocity at time step $n+1$ and n, respectively; M_s is the mass matrix of the solid object and the J operator is formed as follows. Following Batty et al. (2007), for example, the $x-$component of translational forces on the body can be written as:

$$F_x = -\iint_{\partial\Omega_S} p\boldsymbol{n}\, dA = -\iiint_{\Omega_S} \nabla p\, dV\,, \tag{16}$$

where dV denotes the volume differential. Rewriting the above equation into its discretised form in 2D we have

$$F_x \simeq -\sum_{i,j} V_{i+1/2,j} \frac{p_{i+1,j} - p_{i,j}}{\Delta x}\,, \tag{17}$$

where $V_{i+1/2,j}$ is the cell volume occupied by the solid body and it will be discussed in Section 2.4.2. Rewriting Eq. 17 we obtain the $x-$translational part of the operator J:

$$J_{1,(i,j)} = \frac{V_{i+1/2,j} - V_{i-1/2,j}}{\Delta x}\,. \tag{18}$$

The $z-$translational part is formed in the same manner. The torque on a solid object can be expressed as:

$$M = -\iint_{\partial\Omega_S} (\boldsymbol{r} - \boldsymbol{r}_c) \times p\boldsymbol{n}\, dA = \iiint_{\Omega_S} \nabla p \times (\boldsymbol{r} - \boldsymbol{r}_c)\, dV\,, \tag{19}$$

where $\boldsymbol{r}$ is the point of action and $\boldsymbol{r}_c$ is the centre of mass which is also the rotation centre in this paper. Similar to the translational part, the torque part of the operator J can be obtained in the same manner and is given as follows:

$$J_{3,(i,j)} = -\frac{V_{i,j+1/2} - V_{i,j-1/2}}{\Delta z}(x_i - X_c) + \frac{V_{i+1/2,j} - V_{i-1/2,j}}{\Delta x}(z_j - Z_c)\,, \tag{20}$$

where $x_i, z_j \text{and} X_c, Z_c$ are the components of the coordinates of the action point and mass centre, respectively.

Once the operator J is organised, it is straightforward to show that the solid velocity U^{n+1} is actually an explicit expression of pressure via Eq. 15–Eq. 20, which means that the velocity boundary

integral on the right hand side of Eq. 14 can also be expressed as a function of pressure as the velocity at any point on the body surface can be computed by

$$\boldsymbol{u}_{\text{solid}} = \boldsymbol{U}_t + \boldsymbol{U}_w \times \boldsymbol{R}\,, \tag{21}$$

where $\boldsymbol{U}_t$ and $\boldsymbol{U}_w$ are the translational and rotational velocity of the solid, respectively; $\boldsymbol{R} = \boldsymbol{r} - \boldsymbol{r}_c$ represents a vector pointing from the rotation centre to the boundary point. As mentioned above, the solid boundary is discretised into small segments with the same length. Therefore, in a single cell (i, j) the velocity boundary integral of Eq. 14 can be approximated by

$$\int_{G_{ij} \bigcap \partial\Omega_S} \boldsymbol{n} \cdot \boldsymbol{u}_{\text{solid}}^{n+1} dl \simeq \sum_{n_{ij}} \boldsymbol{n}_k \cdot \left(\boldsymbol{u}_k + \boldsymbol{Q}_k(M_s, J, \Delta t, p^{n+1})\right) \Delta l\,, \tag{22}$$

where $\boldsymbol{n}_k$ is the outward pointing unit normal vector; $\boldsymbol{u}_k$ represents boundary velocity due to $\boldsymbol{U}^n$ and $\boldsymbol{f}$; $\boldsymbol{Q}_k$ denotes the boundary velocity transferred from the pressure immediately surrounding the structure; n_{ij} is the total number of boundary segments located inside cell (i, j). Note that $\boldsymbol{n}_k$, $\boldsymbol{u}_k$ and $\boldsymbol{Q}_k$ are all defined at the centre of each boundary segment and n_{ij} is computed at each time step by detecting whether the centre of a segment is located inside the cell or not. This may produce some inaccuracy which is found to be negligible when using an empirical ratio $\Delta l/\Delta x \sim 0.2$. The $\boldsymbol{Q}_k$ term on the right hand side of Eq. 22 connects all the boundary pressures together and it will be added to the left hand side of Eq. 14 modifying the linear equation system for the pressure computation. The linear system is now not necessarily positive definite or symmetric due to the above manipulation as the $\boldsymbol{Q}_k$ term changes between cells due to the differing ratios of cell volumes occupied by solids. However, Press et al. (1992) state that the BCG solver can still be expected to work under these conditions. It is noted that, in Batty et al. (2007), the solid velocity in Eq. 15 is expressed as the kinetic energy of the solids that is directly added to their energy minimization process. In our scheme the velocities on the solid boundary points are further calculated using Eq. 22 for our cut cell based finite volume discretisation of the pressure Poisson equation. In addition, a different approach to compute the solid volume fraction V is required due to the fact that we employ the cut cell technique. This is described in the following section.

After the pressure field is found on the underlying grid, one can update the solid velocity directly using Eq. 15. Alternatively, in this paper the pressure on the grid is firstly interpolated onto the central points of individual boundary segments, and then the fluid force on each segment is calculated

and integrated to obtain the overall force on the solid. Finally, the solid velocity and position are updated using a simple Euler based integration with respect to time. In this way, sub–grid scale accuracy on the calculation of fluid force on the solid is achieved, compared with using Eq. 15, which integrates the fluid force on the grid scale. It is noted that during the solution of the pressure Poisson equation, the $\boldsymbol{Q}_k$ term in Eq. 22 updates the solid velocity using the pressures only in the surrounding fluid cells where the pressure values need to be resolved; therefore, due to the grid discretisation, the hydrostatic case for floating bodies may not be guaranteed, as the fluid cell centres, where the pressure values are stored, are usually not aligned with the solid boundary. To compensate for this, before the interpolation for fluid pressure on the solid boundary segments is performed, the pressure field on fluid cells is linearly extrapolated, considering the effect of gravity, into cells fully occupied by solids, where no pressure values are resolved.

2.4.2. Cell volume occupied by solids

In this section both the current method and the corresponding one employed in Batty et al. (2007) to compute the solid volume fraction V, used in Eq. 18 and Eq. 20 for forming the operator matrix J, are presented. Let us take the different types of cut–cell boundaries as shown in Fig. 2 as examples, where type 1 boundary (left panel) and type 2 boundary (right panel) differ in whether the solid boundary cuts the vertical grid face or not. Within the cell surrounding the horizontal velocity sample $u_{i+1/2,j}$, Batty et al. (2007) use the area of solid region (grey colour part in Fig. 2) as the solid volume fraction, which is required by their variational framework for calculating the kinetic energy in cells surrounding velocity samples. Alternatively, in this paper the approach is to use the fraction ratio θ of the associated vertical cell edge that is occupied by the solid region and multiply it by the cell area, i.e. $V = \theta(\Delta x)^2$. Here, in our case the solid fraction θ is straightforward to compute as it is simply the complement to the open water fraction S mentioned above. Note that for the type 2 boundary θ equals unity in the current approach, as the vertical face $(i + 1/2, j)$ is fully occupied by the solid.

The reason for using this method to calculate the cell volume is because, when the cut cell technique is used for computing fluid pressures, there are no pressure values inside cells that are fully occupied by solids, in which case, the method of Batty et al. (2007) is not appropriate for our scheme in mapping fluid pressure into net forces on solid bodies. However, by using the current approach, the pressures in full solid cells cancel out via Eq. 18 and Eq. 20. For example, in a type 2 boundary, assuming cell $(i + 1, j)$ and $(i + 2, j)$ is fully occupied by solids, then $V_{i+3/2,j} = V_{i+1/2,j} = (\Delta x)^2$, which, according to Eq. 18, results in a zero value for coefficient $J_{1,(i+1,j)}$ of the operator J, and thus eliminates the

requirement of having a pressure value in cell $(i+1, j)$ for the calculation of horizontal fluid force on the solid.

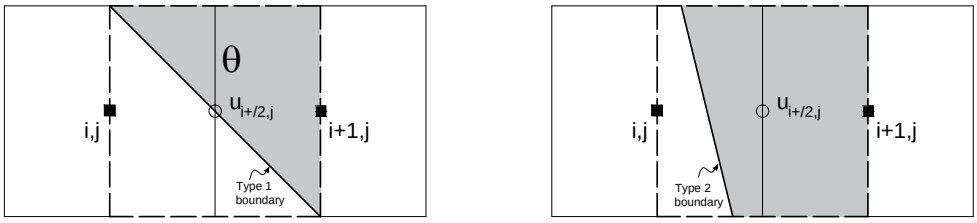

Fig. 2: Cell volume calculation. The dashed line surrounded area represents the cell surrounding velocity sample $u_{i+1/2,j}$ with solid region indicated by the grey colour.

2.4.3. Free–surface tracking

The particles in the PICIN model are used not only for advecting the divergence–free velocity field but also to track the free surface. In PICIN the boundary conditions are resolved on the Eulerian grid during the solution of the pressure Poisson equation. Following Gibou et al. (2002), we impose a second–order accurate free surface boundary condition on the free surface defined by the particle positions. This is achieved via a SDF constructed at the centre of every single grid cell with respect to the free surface.

Assuming the SDF $\phi < 0$ inside the fluid phase and $\phi > 0$ outside the fluid domain, $\phi = 0$ thus represents the free–surface contour. We first use the method of Zhu and Bridson (2005) to compute SDF value on the closest air cells to the free surface based on the particle position:

$$\phi_{ca}(\boldsymbol{x}) = |\boldsymbol{x} - \bar{\boldsymbol{x}}_0| - r_0 \tag{23a}$$

$$\bar{\boldsymbol{x}}_0 = \frac{\sum_i \boldsymbol{x}_i W(k_h, \boldsymbol{x} - \boldsymbol{x}_i)}{\sum_i W(k_h, \boldsymbol{x} - \boldsymbol{x}_i)} \tag{23b}$$

where ϕ_{ca} represents the SDF value on the closest air cell to free surface; $\boldsymbol{x}$ is the particle position vector; r_0 denotes a constant value for particle radius; W is the cubic spline kernel function (Monaghan and Lattanzio, 1985) with k_h the so–called kernel length determining the neighbourhood of involved particles. This technique can reconstruct the SDF of an isolated particle as well as flat or smooth surfaces but may have disadvantages in concave regions where $\bar{\boldsymbol{x}}$ may end up outside the surface (Zhu and Bridson, 2005). In practice, effects of this drawback are negligibly small when the resolution is high as the neighbourhood of particles used are just within one or two cell lengths. Once this step is completed along all the free surface boundary, those seed SDF ϕ_{ca} are then spread out onto cells along

the free surface by solving the Eikonal equation:

$$|\nabla\phi(\boldsymbol{x})| = f(\boldsymbol{x}), \qquad \boldsymbol{x} \in \Omega \tag{24a}$$

$$\phi(\boldsymbol{x}) = \phi_{ca}(\boldsymbol{x}), \qquad \boldsymbol{x} \in \Gamma(\boldsymbol{x}, t) \in \Omega \tag{24b}$$

$$\phi(\boldsymbol{x}) = \phi_b(\boldsymbol{x}), \qquad \boldsymbol{x} \in \partial\Omega \tag{24c}$$

where $f(\boldsymbol{x})$ equals -1 (inside the fluid domain) or 1 (outside the fluid domain); Ω and $\partial\Omega$ are the computational domain and the domain boundary, where a boundary value of SDF ϕ_b is given; $\Gamma(\boldsymbol{x}, t)$ represents the closest air cell boundary with ϕ_{ca} being the SDF value computed from the above boundary reconstruction approach. Eq. 24 are solved using the fast sweeping approach proposed in Zhao (2004), which is efficient and straightforward. In fact, to make this scheme more efficient, in PICIN the SDF is spread to a cell band around $\Gamma(\boldsymbol{x}, t)$ rather than the whole domain Ω.

It is worth mentioning that the SDF with respect to the solid boundary is constructed on the cell vertices in the same manner discussed here.

2.5. Algorithm

In summary, the modified PICIN model has the following steps for the time integration:

(1)Update the positions of both fluid particles and solid structures independently.

(2)Transfer the velocity from particles to the grid and compute tentative velocities for relevant cell faces.

(3)Construct the SDF at cell centres for imposing the free surface boundary conditions and at cell vertices for applying the solid boundary conditions.

(4)Construct and resolve the modified pressure Poisson equation using the coupling scheme introduced in this paper.

(5)Project the tentative velocity to a divergence–free velocity field using pressures.

(6)Update the velocities of both solid objects and fluid particles separately.

(7)Update the time step controlled by the Courant number and repeat step (1) to (7).

3. Numerical wave tank in PICIN

A numerical wave tank is set up following the methodology described in Chen et al. (Unpublished results). Numerical waves are generated by a Piston–type wavemaker and absorbed at the downstream

end of the tank via a relaxation zone method. Linear wave theory is used for wave generation by giving a prescribed velocity wall boundary which is resolved via Eq. 14. For wave absorption, the relaxation zone approach of Jacobsen et al. (2012) is adopted; the velocity of particles at the end of the computational domain is forced to be the desired analytical solution, which in our case is water at rest. Both of these techniques are validated for regular wave generation and absorption within the PIC framework in Chen et al. (Unpublished results) and have been used for all test cases in this paper.

For the test case in Section 4.3, a focused wave generation is required where the free–surface elevation can be expressed following Zhao and Hu (2012):

$$\eta(x,t) = \sum_n a_n \cos(k_n(x - x_f) - \omega_n(t - t_f)) \,, \tag{25}$$

In which, following Chen et al. (2014b),

$$a_n = A_f \frac{S(\omega_n)\Delta f}{\sum_n S(\omega_n)\Delta f} \,, \tag{26}$$

where k_n and ω_n are the wave number and wave frequency for the nth wave component, respectively; x_f, t_f and A_f are the focused position, focused time and focused wave crest value; $S(\omega)$ is the wave energy spectrum representing wave energy distribution. In order to compare the results with Zhao and Hu (2012), the Joint North Sea Wave Project (JONSWAP) spectrum form proposed in Goda (1999) is used in this paper:

$$S(f_i) = \beta_J H_{1/3}^2 T_p^{-4} f_i^{-5} e^{[-5/4(T_p f_i)^{-4}]} \cdot \gamma^{\exp[-(f_i T_p - 1)^2/2\sigma^2]} \tag{27}$$

with

$$\beta_J = \frac{0.06238(1.094 - 0.01915 \ln \gamma)}{0.230 + 0.0336\gamma - 0.185(1.9 + \gamma)^{-1}} \,, \tag{28}$$

and $\gamma = 3.3, \sigma = 0.07(\omega < \omega_p)$ and $\sigma = 0.09(\omega \geq \omega_p)$, where f_i is the frequency of wave component and T_p is the peak frequency of spectrum.

With the free–surface elevation determined from Eq. 25, it is straightforward to obtain the moving velocity of the Piston–type wavemaker at location x_0 according to linear wavemaker theory (Dean and Dalrymple, 1991):

$$U_b(x_0,t) = \sum_n \frac{\omega_n}{T_r(\omega_n)} a_n \cos(k_n(x_0 - x_f) - \omega_n(t - t_f)) \,, \tag{29}$$

with

$$T_r(\omega_n) = \frac{4\sinh^2 k_n h}{2k_n h + \sinh 2k_n h}\,, \tag{30}$$

where T_r is the transfer function and h is the water depth. We note here that the position of the Piston–type wavemaker at each time step is given by integrating Eq. 29 with respect to time.

4. Test cases

In this section a number of test cases are presented in which the new fluid–solid interaction scheme, as well as the PICIN model, is validated against experimental data and other numerical results. Emphasis is given to the validation of the new scheme for hydrodynamic processes occurring in the vicinity of coastal and offshore structures by three benchmark cases; these are: i) Wave force on a fixed submerged cylinder (Dixon et al., 1979), ii) 1–DoF roll motion of a rectangular box under regular wave conditions (Jung et al., 2006), and iii) 2–DoF floating structures under extreme wave conditions (Zhao and Hu, 2012).

4.1. Wave force on a fixed horizontal cylinder

This test case was experimentally studied by Dixon et al. (1979) in order to improve Morison's equation on wave force calculation for fixed, horizontal, partially submerged cylinders. This case was also numerically investigated by Westphalen et al. (2014) using a state–of–the–art weakly compressible SPH (WCSPH) method. We compare our model results with both the experimental and the numerical data, in order to assess the performance of the numerical scheme in terms of calculating dynamic pressures and forces. We impose a no–slip boundary condition for the solid boundary of the investigated structure and free–slip boundary conditions on the computational domain walls as well as boundaries of the wavemaker, and these are set the same for all test cases in this paper.

A cylinder, with diameter D, is initially submerged in still water of depth h. The cylinder submergence, d, is defined as the distance of the centre of the cylinder from the free surface. Regular waves of amplitude A and period T are generated to interact with the cylinder. We select two test conditions found in Dixon et al. (1979) and Westphalen et al. (2014). The key parameters of the tests are shown in Table 1, where the cylinder diameter is $D = 1$ m in current simulations.

In the numerical model, regular waves are generated using the techniques presented in Section 3 and the length of damping zone is at least 2.5 times wave length in both tests (see Table 1) to maintain the wave reflection at around 1% (Chen et al., Unpublished results). The numerical wave tank is 150

Table 1: Characteristics of investigated sub–merged cylinder and incident wave.

	Test condition 1	Test condition 2
d/D	-0.3	0
A/D	0.2	0.5
kA	0.08	0.2
kh	1.61	1.61

*k is the wave number.

m long and 5 m high in total with the cylinder placed at 70 m from the wavemaker. Four sets of computational grid sizes are used for the convergence test for test condition 1, and $\Delta x = \Delta z = D/20$ is chosen to produce data for comparison for both test conditions, resulting in about 958,000 particles with a grid resolution of 3000×100. The time step is dynamically controlled by setting the maximum Courant number to 0.5, which is used throughout this paper unless stated otherwise. It took about 10.3hrs for 66s simulation (20 wave periods) for test condition 1 at an Intel(R) Core(TM) i7–4600U CPU@2.1GHz laptop.

The non–dimensional vertical wave force $F_z^{'}$ on the cylinder is calculated for comparison:

$$F_z^{'} = \frac{F_z}{1/4\pi D^2 l \rho g}\,, \tag{31}$$

where F_z is the measured vertical wave force and l is the length of cylinder. Note that the vertical wave force F_z is calculated by subtracting the buoyancy force of the submerged cylinder with water at rest from the overall vertical wave force which, in the experiment, was measured over one cycle starting at the point when the water line would have crossed the still water level going upwards at the position of the front edge of the cylinder, in the absence of the model.

The convergence test and comparison of the vertical wave force with experimental data and the WCSPH model are shown in Fig. 3, for test condition 1 ($d/D = -0.3$). The data were sampled when the waves are fully developed and the vertical wave force reaches the steady state (see Fig. 3(a)). Fig. 3(b) shows a comparison of the results for four sets of grid sizes, and Table 2 presents the L^2 error norm for data of 20 wave periods and the order of convergence. It is noted that the results run with the grid size $D/25$ were used as the reference data, as this is the finest grid that almost reaches the limitation of our computational resources. It can be seen that the results are convergent when the grid size is $D/20$.

Snapshots of the free surface and horizontal velocity field during a typical wave cycle for test condition 1 are plotted in Fig. 4. Together with Fig. 3(c), it can be found that, for each cycle, the

vertical wave force first increases as the wave crest surges onto the cylinder and then decreases sharply to a negative value when the wave trough comes into action. Also, it can be seen from Fig. 3(c) that the agreement of results between current numerical model and the experiment is very good. Compared with the WCSPH model, our PICIN model predicts better results for both the amplitude and phase of the vertical wave force. Similarly, the vertical wave force comparison and snapshots of the free surface and pressure field for test condition 2 ($d/D = 0$) are shown in Fig. 5 and Fig. 6, respectively. For test condition 2, the magnitude of the wave force is relatively large as the wave condition is much more violent and the cylinder is above the water surface during most of the wave period. It can be seen from Fig. 5 that the numerical results agree well with the experimental data, and our results seem to be better around the second peak of the vertical wave force.

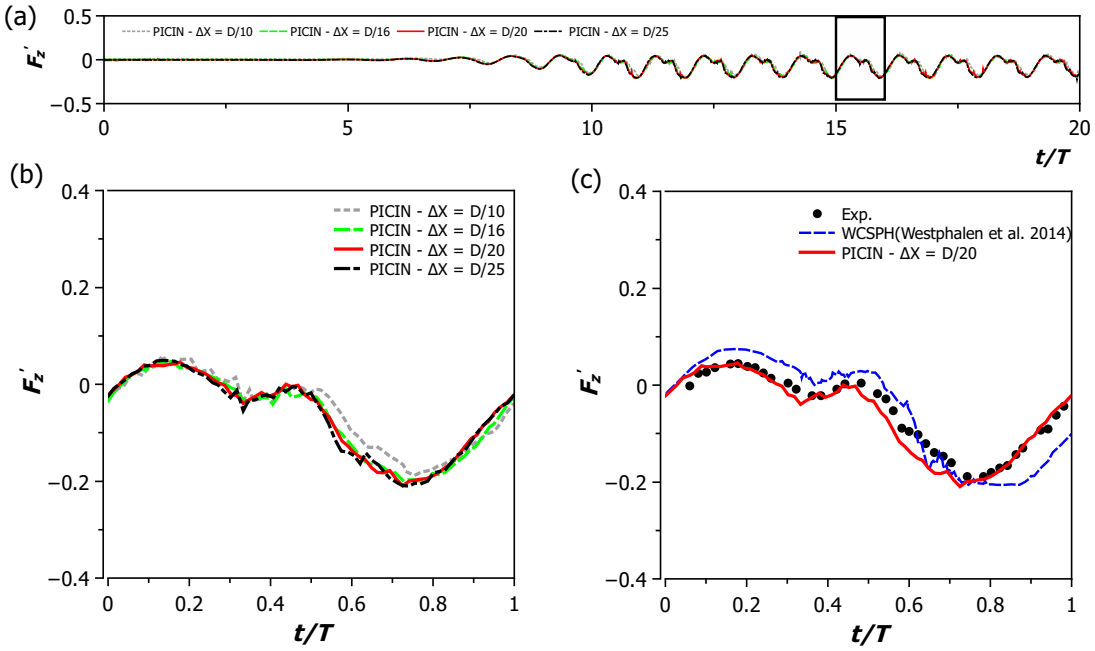

Fig. 3: Time history of non–dimensional vertical wave force on the cylinder for test condition 1 ($d/D = -0.3$). (a) Numerical data of 20 wave periods from PICIN. (b) Zoom in comparison for results from different grid sizes (c) Zoom in comparison between experimental and selected numerical results.

Table 2: Convergence test for vertical wave force on cylinder for test condition 1 in test case 1.

Grid size	L^2 error norm	Order of convergence
$D/10$	1.033	–
$D/16$	0.481	1.62
$D/20$	0.312	1.95

The development of spikes in the wave force signal is noted for both numerical models. While this is the case for the WCSPH model used by Westphalen et al. (2014), Skillen et al. (2013) demonstrate

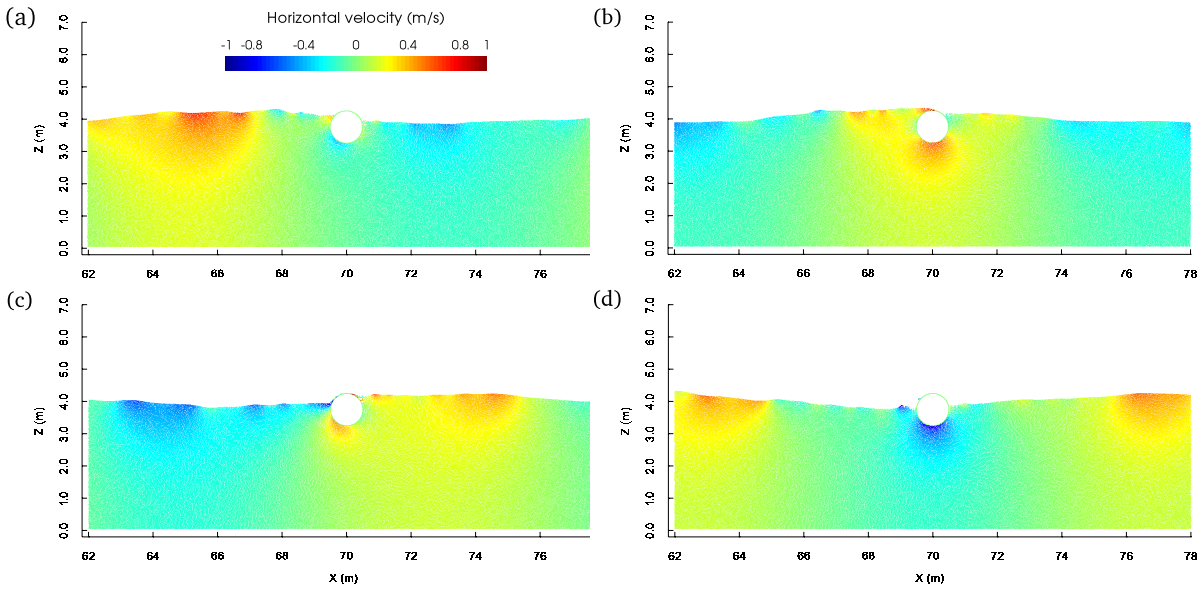

Fig. 4: Snapshots of wave interaction with fixed cylinder for test condition 1 ($d/D = -0.3$) starting from $t = 0.25T$ (a) with an approximately $0.25T$ time interval.

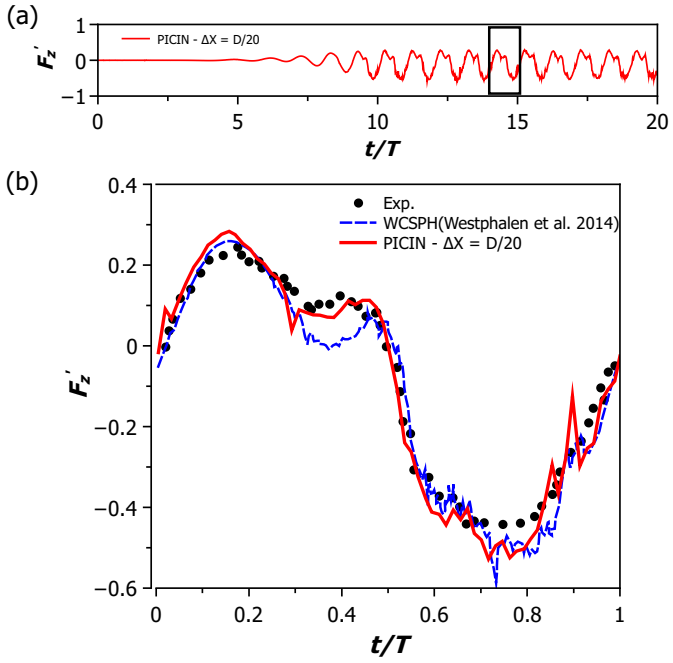

Fig. 5: Time history of non–dimensional vertical wave force on the cylinder for test condition 2 ($d/D = 0$). (a) Numerical data of 20 wave periods from PICIN. (b) Zoom in comparison between experimental and selected numerical results.

that this noise can be reduced significantly by an approach based on the incompressible SPH model. In our case this is probably due to the use of fluid particles to track the free surface as well as indicate the fluid region. In cases involving violent fluid–solid interactions, a fluid cell will occasionally have only

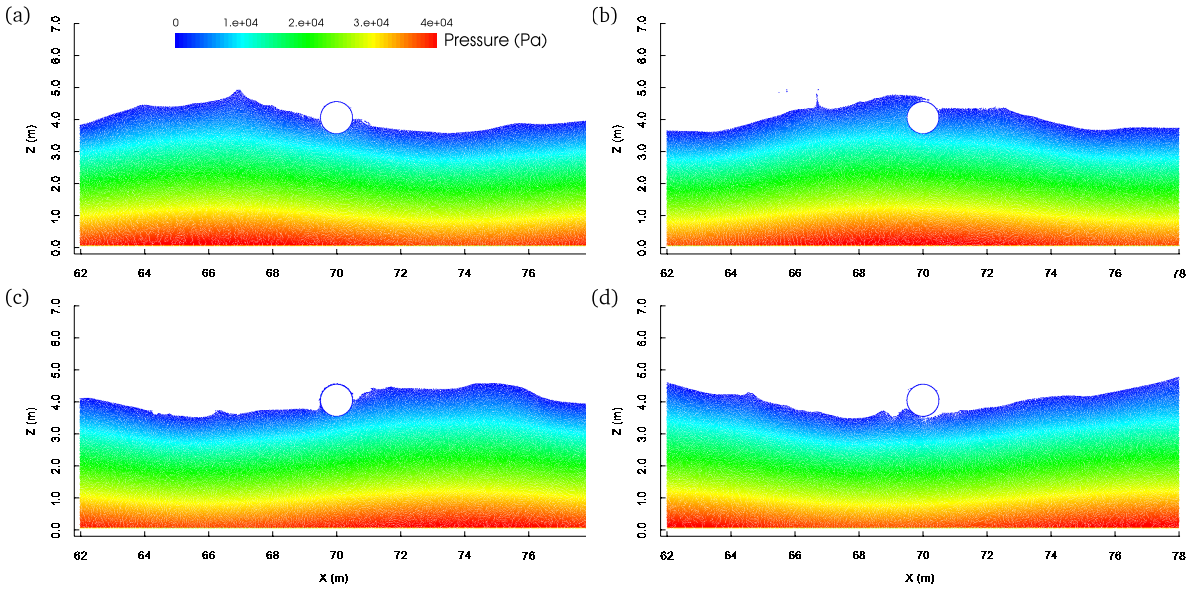

Fig. 6: Snapshots of wave interaction with fixed cylinder for test condition 2 ($d/D = 0$) starting from $t = 0.25T$ (a) with an approximately $0.25T$ time interval.

one or two particles inside, which may lead to pressure fluctuation due to a lack of resolution. Further improvements could be made by using phase averaging techniques during result post processing that may smooth some of these spikes.

4.2. Roll motion of a rectangular box

We use this test case to validate the capability of the numerical model in simulating 1–DoF roll only box motion under regular wave conditions. This is an example of the situation where the viscous damping is particularly important in controlling the box motion near the resonance frequency(Downie et al., 1988). To ensure 1–DoF motion for this case in our fluid–solid interaction scheme, the surge and heave motion of the structure and relevant translation velocities in Eq. 21 are simply set to zero.

This case was experimentally studied by Jung et al. (2006) with an emphasis on the vortex interaction with the roll motion of the box. The experiments were carried out at Texas A&M University and a sketch of the experimental set up is presented in Fig. 7. The physical model was performed in a 35 m long and 0.9 m wide wave tank with water depth set to be 0.9 m. A rectangular box with dimensions of 0.3 m long, 0.1 m high and 0.9 m wide is fixed onto the tank and only allowed to rotate along its centre of gravity (0.05 m from the keel) such that the flow can be considered as 2D. The draft of the box is 0.05 m and the moment of inertia of the actual mass of the box is $I = 0.236$ kg·m^2. In addition, the fluid velocity in the experiment was measured by the particle image velocimetry (PIV) technique. The range of the tested wave conditions for the numerical study were selected according to

Jung et al. (2006) and these are shown in Table 3.

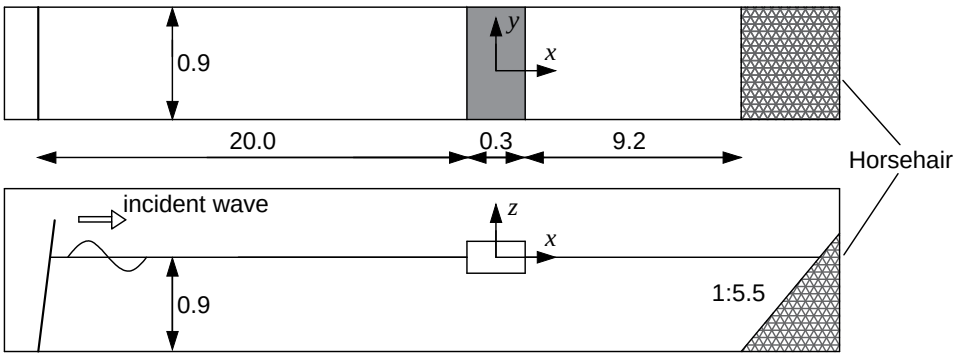

Fig. 7: Sketch of experimental wave tank in Jung et al. (2006) (Unit: m).

Table 3: Experimental wave conditions.

Test	Frequency ω(rad/s)	Height H(m)	kA
1	8.98	0.029	0.1191
2	7.85	0.029	0.0912
3	7.39	0.033	0.0919
4	6.76	0.040	0.0931
5	6.28	0.044	0.0887
6	5.24	0.060	0.0849
7	4.49	0.061	0.0653

Simplifications are made for the wave tank in our numerical model. First, the horizontal position of the roll box in our numerical model is not fixed at $x = 20$ m as shown in Fig. 7, instead, we change the position according to wave conditions and thus change the length of wave tank correspondingly. In particular, for test $1 \sim 5$ the length of numerical wave tank is 20 m with the floating box placed at a distance of 14.5 m from the wavemaker and for test 6 and 7 these are 30 m and 20.5 m, respectively. By placing the floating body closer to the wavemaker, we ensure that the roll motion will be fully developed before being contaminated by secondary reflections from the wave paddle, as active absorption has not been yet implemented in the PICIN model, and having a shorter computational domain is also beneficial in terms of minimising any numerical diffusion that may be present. Second, instead of using a horsehair structure to damp out the wave at the end of wave flume, we used an absorption zone as discussed in Section 3, which was at least 2.5 times the wave length of each wave condition. The cell size used for all tests in this case is $\Delta x = \Delta z = 0.01$ m, resulting in a total cell number ranging from 270,000 to 405,000. The CPU cost varies from case to case; for example, it took about 10.9 hrs for 43 seconds of simulation at an Intel(R) Core(TM) i7–4600U CPU@2.1GHz laptop for the test ($\omega = 5.24$

rad/s) with the maximum 405,000 cells and 1,061,000 fluid particles.

A free decay test of the roll box is first carried out in calm water. The rectangular box is initially given an inclination with an angle of 15 degree and released to roll freely. As shown in Fig. 8, during each cycle the roll motion decayed because of the damping effect. It can be observed that the roll motion is damped out much faster in experiment than the numerical simulation. For further comparison, following Jung et al. (2006), the free decay time history is used to calculate the loss of roll amplitude against mean angle of roll in each swing, from which the slope of the linear fit line is used for computing the damping coefficient b (Bhattacharyya, 1978):

$$b = \frac{K_1 T_N \Delta \overline{GM}}{\pi^2}, \tag{32}$$

where K_1 is the slope of the linear fit line; T_N is the natural period; Δ is the volume of displacement; $\overline{GM}$ is the metacentric height, which is defined as the distance between the centre of gravity and the metacentre of the floating structure, and in this case is equal to 0.125 m. By averaging the time interval between each peak of the free decay curve we obtain the natural frequency of the roll box is $\omega_N = 6.91$ rad/s which is slightly higher than the value from experiment, 6.78 rad/s, and via Eq. 32 we have a damping coefficient $b = 0.293$ which is less than 0.519 from the experiment. We note that the smaller damping coefficient in this case has also been shown in the results of other numerical models; e.g. Nematbakhsh et al. (2013); Ghasemi et al. (2014); Chen et al. (2014a). As for our model, this smaller damping coefficient in the numerical simulation may be, to some extent, due to the absence of the extra friction damping from the physical devices used in the experiment. More importantly, the model does not include the strong turbulent dynamics developed during the box roll motion as demonstrated in the experiment of Jung (2005), which, without getting into the details, will increase the effective viscosity of the fluid and cause more energy dissipation in the system. As a 2D numerical approach, the current model cannot directly resolve the turbulent effects that correspond to the physical processes. In order to resolve turbulent effects for the 2D model, the Reynolds–Averaged Navier Stokes equations, coupled with a transport model for the turbulence properties (e.g. k–epsilon or k–omega) (Wilcox et al., 1998), could be used for future investigation. It is also worth noting that since currently our model does not use a turbulence closure model, turbulent boundary layers are not properly resolved. This could be an additional source of the large discrepancy between experimental and modelled results as shown in Fig. 8. Fig. 9 presents the comparison for the results of steady state roll motion magnified by kA under different wave frequencies. As can be observed, our results are overall more energetic than those of

experiment, which is consistent with the damping coefficient b from our numerical model being smaller than the experimental one, due to the reasons given above.

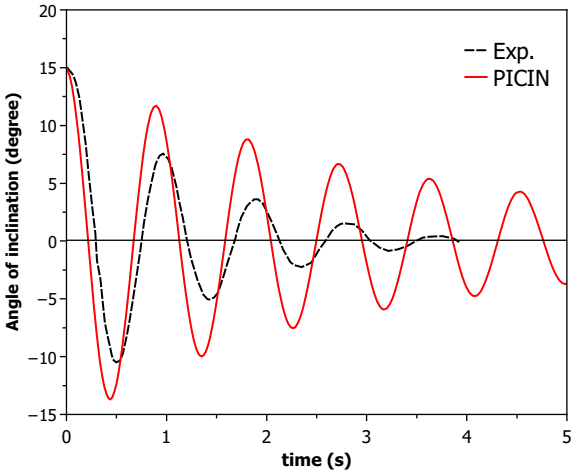

Fig. 8: Time history of roll in the free decay test.

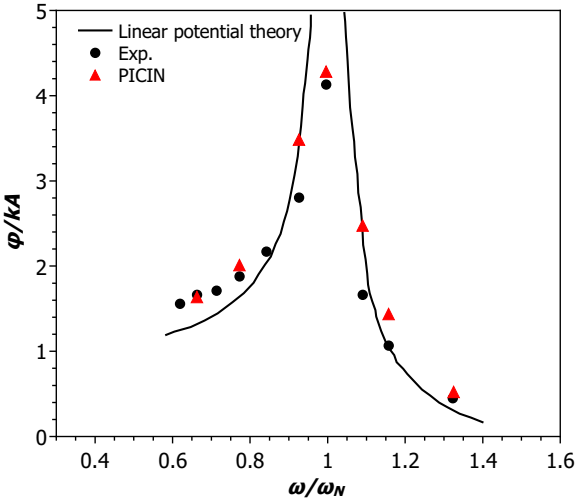

Fig. 9: Magnification factors for roll motion.

Flow separation at the corner of the structure also has an important effect for wave frequencies lower than the natural frequency of the free rolling structure, in which case, as pointed out in Jung et al. (2006), the vortex shedding due to flow separation at structure corners leads to an amplification of the roll motion rather than a damping out of the motion. We observed similar phenomena from our numerical results. Fig. 10 presents a snapshot of both vorticity field and velocity field interpolated on the particles for a low wave frequency case $\omega = 5.24$ rad/s ($\omega/\omega_N = 0.77$). Similar to that discussed in Jung et al. (2006), after the box reaches the maximum angle of clockwise motion, a strong negative

vortex (clockwise) is generated when the box rolls back (Fig. 10(a) to (b)). This negative vortex, initially tending to damp out the roll motion, is quickly reversed, and then a strong positive vortex is formed and stays ahead of the structure roll direction (Fig. 10(c) to (e)) due to the separation of relatively high speed flow at the structure corners. This positive vortex actually helps the repeated clockwise roll motion. Similarly, when the box starts the clockwise motion again, a negative vortex is formed ahead of the moving direction of the box due to the separation of high speed flow (Fig. 10(f) to (g)), which again helps the clockwise roll motion. So, during most stages of the cycle the generated vortices are actually enhancing the roll motion rather than damping it, which results in a larger roll motion than the result obtained by linear potential flow theory in the low frequency area (see Fig. 9), where there is enough time for the vortices to develop.

4.3. Floating body under extreme wave conditions

This test case concerns the simulation of the coupling heave and roll motion of a floating body under both regular wave and extreme wave conditions. This case was previously investigated by Zhao and Hu (2012) where experimental data as well as the numerical results from Constrained Interpolation Profile (CIP) method are available for comparison. The experiments were carried out in a wave tank at the Research Institute for Applied Mechanics (RIAM) Kyushu University, Japan. The wave tank is 18 m long, 0.3 m wide and 0.7 m high and is equipped with a plunge–type wave generator and a wave absorbing device at each end. The water depth is fixed at $h = 0.4$ m throughout the experiments. Fig. 11 shows a schematic of the experimental set–up. The floating body is a symmetrical rectangular box with a deckhouse and the major parameters of this structure are given in Table 4. The floating body is connected with a heaving rod through the rotational joint which is initially placed at the free surface of calm water. The heaving rod can move smoothly through the slider mechanisms fixed on guide rails on the top of the tank such that the floating structure can move in heave and roll motion with surge motion being restricted. The mass of the floating body and heaving rod are $m_1 = 14.5$ kg and $m_2 = 0.276$ kg, respectively. Wave gauges are placed at the upstream of floating body to measure free–surface elevation and a pressure sensor is installed on the seaward side wall of the deckhouse at a height of 0.01 m above the deck (see Fig. 11) to monitor the impact pressures.

For this test case, both regular wave and focused wave were generated in the experiment. The regular wave period is chosen to be $T_w = 1$ s and the wave amplitude is $A = 0.031$ m. For the focused wave, the peak frequency is $f_p = 1.0$ Hz with frequency of wave components ranging from 0.6 to 1.6 Hz. The focused position, time and amplitude are set at $x_f = 7.0$ m, $t_f = 20$ s and $A_f = 0.06$ m,

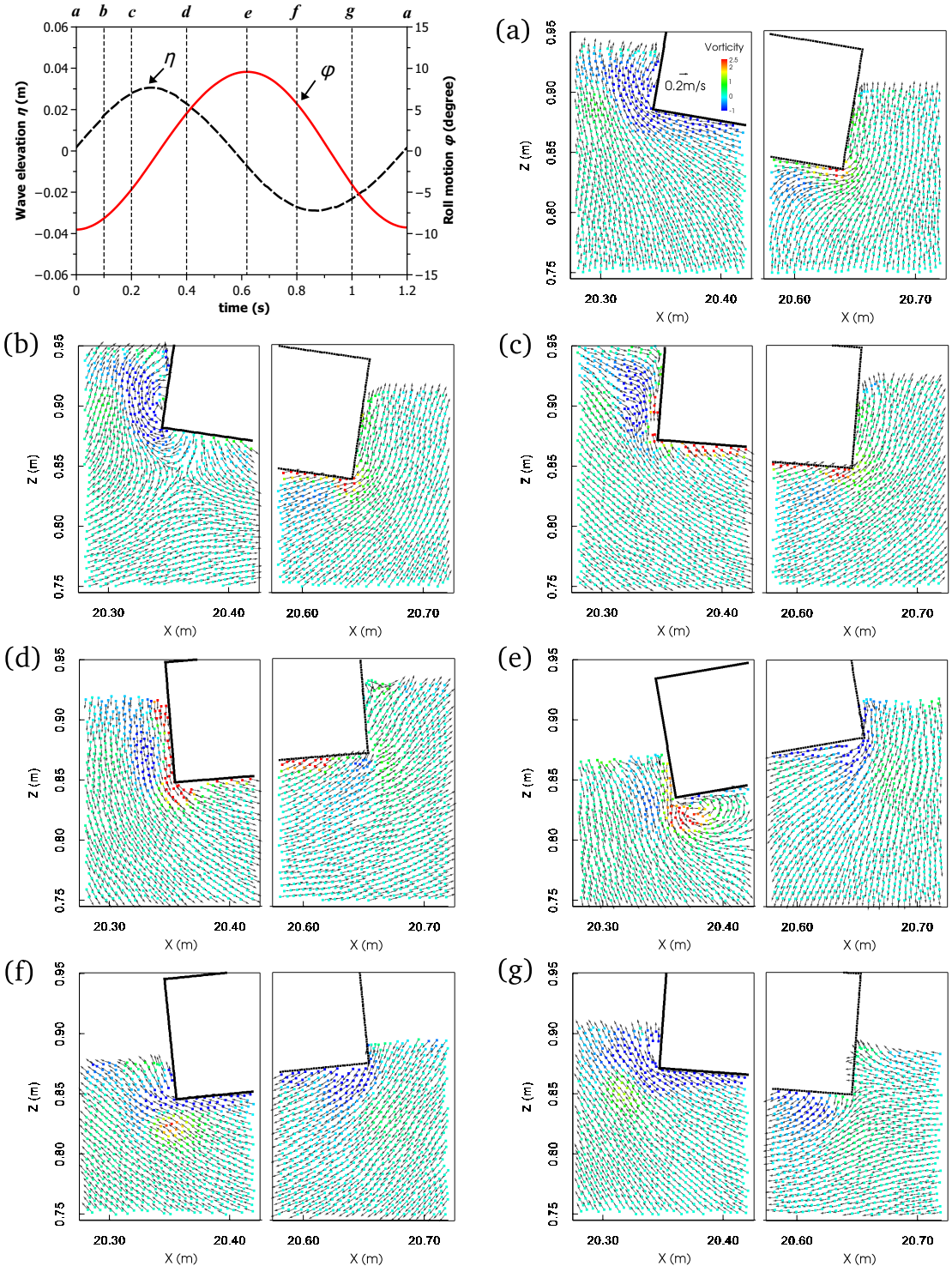

Fig. 10: Measurements for $\omega = 5.24$ rad/s ($\omega/\omega_N = 0.77$) wave. The top left panel shows free–surface elevation of the incident wave in the absence of model and roll angle of the box with phases a–g corresponding to each of the velocity and vorticity snapshots. The vorticity is normalised by $9.81^{1/2}s^{-1}$.

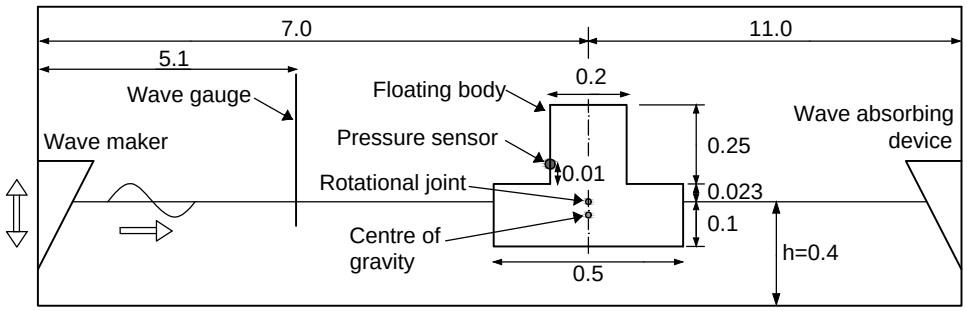

Fig. 11: Sketch of experimental set up in Zhao and Hu (2012) (Unit: m).

Table 4: Major parameters of the floating structure.

Item	Value (m)
Length	0.5
Breadth	0.29
Draft	0.1
Centre of gravity (from the bottom)	0.0796
Gyration radius	0.1535

respectively. In the numerical model, 29 wave components are used for the generation of the focused wave. Note that the wave steepness for the regular wave is 0.133, and it is 0.258 for the focused wave using the wave number of the peak frequency component and the focused wave amplitude; these imply that weakly and strongly nonlinear waves are used for this test case, respectively.

To save CPU time for current numerical simulation, following Zhao and Hu (2012), the distance from the centre of floating structure to the downstream end of the tank is reduced to be 7 m with 6 m dedicated to the wave absorption zone. Both the regular waves and focused waves are generated using the piston–type wavemaker technique as discussed in Section 3. The grid size is $\Delta x = \Delta z = 0.00625$ m, resulting in a cell resolution of 2264×120 with about 574,000 fluid particles. The maximum Courant number is 0.4 for the time step control and it took approximately 8.3 hrs to complete a total 30 seconds of simulation at an Intel(R) i7-4600U CPU@2.1GHz core laptop.

Fig. 12 shows comparisons of both the time history and the corresponding frequency spectrum of floating body motion and free–surface elevation under regular wave conditions. On the top sub–panel of the time history comparison (left panel in Fig. 12), the evolution of free–surface elevation in time is presented, in the absence of the floating structure, with the data being recorded at the location of the structure. This time series is presented for completeness, as no experimental data are available. Since a large wave amplitude is used in this test case, the wave–on–deck occurs in both the current numerical simulation, CIP modelling and experiment (Zhao and Hu, 2012). From the comparison of

time history, it can be seen that our model under predicts the averaged amplitude of heave motion by about 7.8% but over predicts the averaged amplitude of roll motion by about 4.2%, which may be mainly due to that some effects of wave–on–deck that occurred in the experiments are not fully resolved by the current 2D numerical model. We note that this also happened for numerical results from the CIP model as discussed in Zhao and Hu (2012). However, our PICIN model gives much better results than the CIP model in terms of the wave elevation at $x = 5.1$ m in the presence of the floating structure (refer to Fig. 13 in Zhao and Hu (2012)), where the free surface is influenced by both the incoming wave and the reflected wave from the floating body. We note that minor discrepancies in phase are shown between our numerical results and experimental data for the time history of floating body motions. The reasons for this are still unclear at the time of writing. For the comparison of frequency spectrum (right panel in Fig. 12), it can be seen that the current model clearly captures the nonlinear effects of the wave–wave interaction due to the large wave steepness; for example, the second–order harmonic is presented in the generated regular waves (see the top sub–panel). Also, in both the experimental and numerical results, the second– and third–order harmonics are found in the wave elevations influenced by the wave–structure interaction (see the bottom sub–panel). It is also found that some low frequency components around $f = 0.5$ Hz of the floating body motions are only produced in the current numerical simulation. This is probably caused by the occurrence of pressure spikes, as mentioned in Section 4.1, and it also partly accounts for the discrepancies as found in the time history comparison of floating body motions. Nevertheless, the overall agreement between the experiment and numerical simulation is good.

For the focused wave case, the input of focused wave amplitude and time are slightly adjusted in the numerical model in order to make the wave groups focus with a crest value of 0.06 m at x_f =7 m, where the floating body is placed. In the absence of a floating body, the numerical focused wave is first generated and the wave profile at the focused position is compared with the experimental data as shown in the top sub–panel of the time history comparison (left panel of Fig. 13). This configuration of focused wave generation is then used for the investigation of wave interaction with the floating body. The numerical time history results along with the corresponding frequency spectra are compared with the experimental data, as shown in Fig. 13. From the time history comparison, it is found that the PICIN model underestimates the nonlinear heave motion of the floating body by about 16.8% and 21.7% for the trough and the peak respectively, which may be due to the wave–on–deck effects as discussed in the regular wave case. We note that here the nonlinearity in the floating body heave

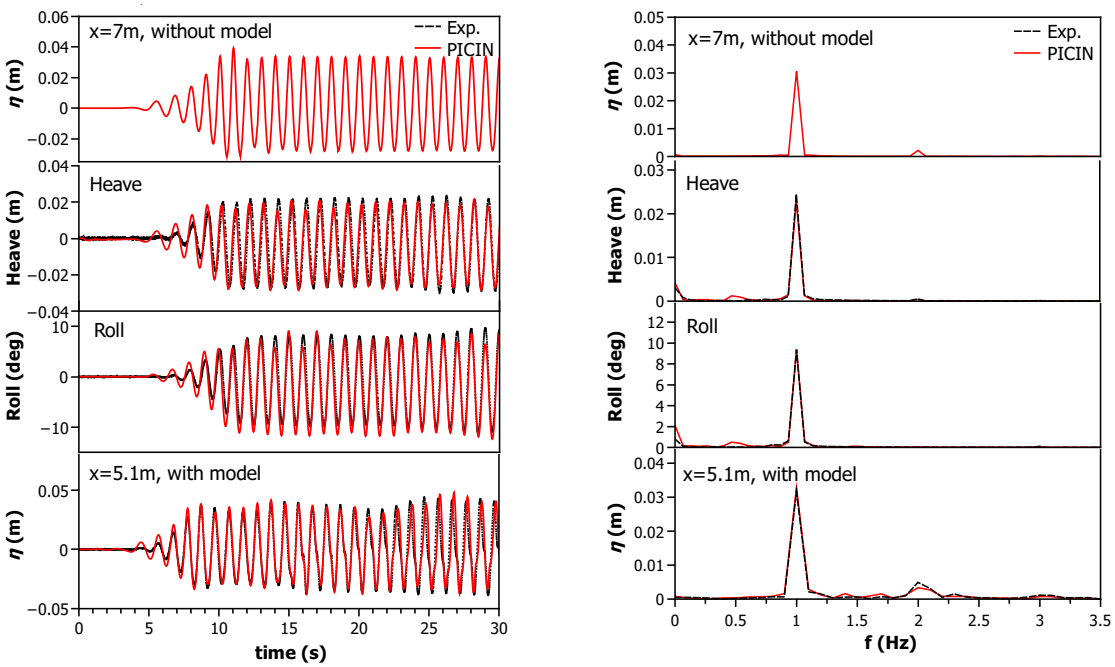

Fig. 12: Time history (left panel) and frequency spectrum (right panel) comparison for regular wave condition ($A = 0.031$ m).

motion is probably caused by the green water effect, violent wave impact on the structure and induced complex free–surface motions described below. Nevertheless, the overall agreement for the floating body motion, as well as wave elevation at $x = 5.1$ m, is good. Moreover, from the spectrum analysis (right panel of Fig. 13), it can be seen that the current model captures the energy distribution for both the focused wave and floating body motions across all frequency ranges, including both lower and higher order harmonics.

Fig. 14 shows a set of numerical snapshots at the same time instant with the experimental photographs. We can see that the focused wave reaches the floating body and propagates on the deck, leading to a flow impact on the deckhouse. The impact jet runs up and then overturns due to gravity, resulting in violent wave breaking in front of the body. The PICIN model captures the major processes of this violent fluid–solid interaction well, compared with the experiment, although it is noted that our results seem to occur slightly earlier in time. The slightly earlier arrival of green water could be due to that the structure heave and roll motion predicted by the model are slightly earlier than those of the experiment (see the left panel in Fig. 13). This is probably caused by the discrepancy in the generated numerical and experimental focused waves. We found that it is very challenging for the model to produce exactly the same focused wave as the experiment.

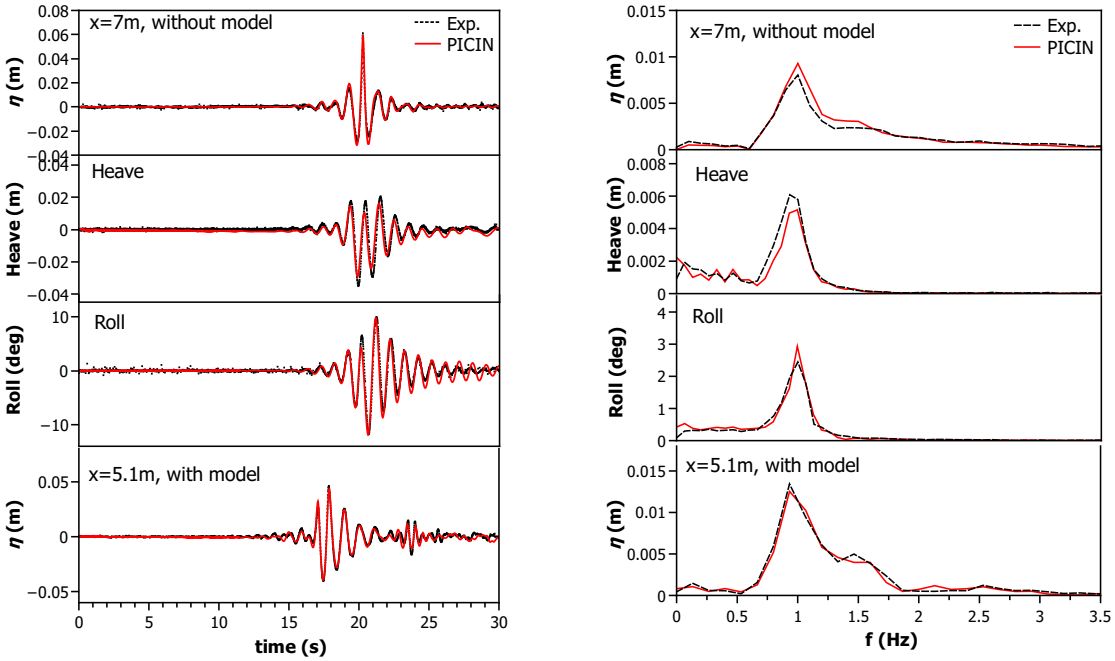

Fig. 13: Time history (left panel) and frequency spectrum (right panel) comparison for focused wave condition ($A_f = 0.06$ m).

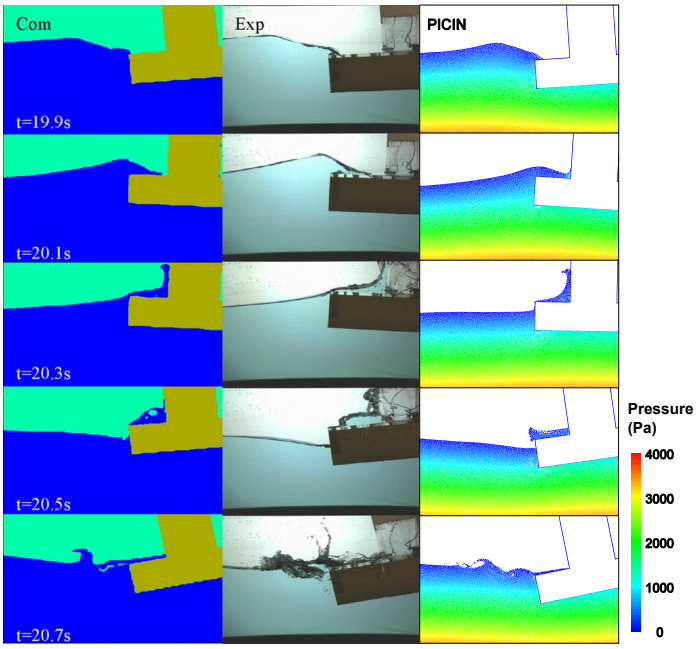

Fig. 14: Comparison between the CIP method (left) and experiment (middle) (reprinted from Zhao and Hu (2012), Copyright (2012), with permission from Elsevier), and PICIN (right) for free–surface elevation and structure motion under the focused wave condition ($A_f = 0.06$ m).

The time history of fluid pressure on the pressure sensor (see Fig. 11) is also compared between experimental and numerical data and it is shown in Fig. 15. From Fig. 15, it is observed that PICIN

captures the variation trend of the pressures well for both the regular and the focused wave conditions. In particular, peak pressures during the regular wave conditions are very well captured, although the experimental data show that during wave run–down there is a higher residual pressure due to the slower water drainage than that predicted by the numerical model. The same effect is observed in the focused wave case for $t > 20.5$ s, and it is also confirmed by the observations in Fig. 14. The two pressure peaks developing in the focused wave case are underestimated by the PICIN model, while the trend is well captured. This underestimation is probably due to the single phase approach used in the numerical model, as the role of air is believed to be important in the development of impulsive pressures (Lind et al., 2015).

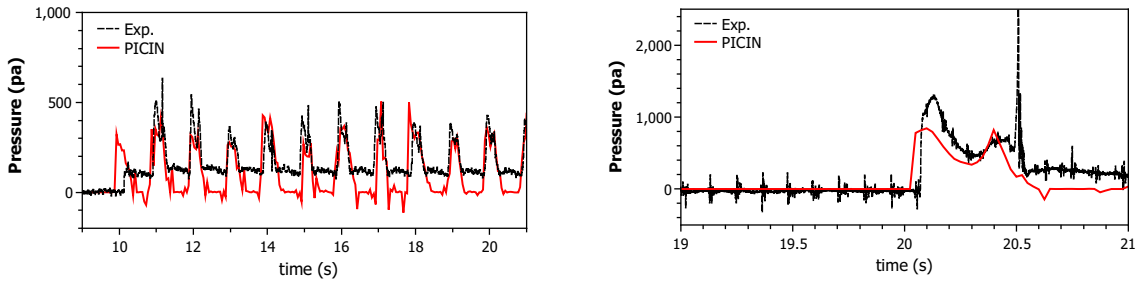

(a) Regular wave, $A = 0.031$ m

(b) Focused wave, $A_f = 0.06$ m

Fig. 15: Pressure Comparison for different wave conditions.

5. Conclusions

This paper presents modifications to the PICIN model of Kelly et al. (2015) that allow for the simulation of arbitrarily configured (surface piercing) floating bodies. The PICIN model has been updated so that transfer of data from the grid to the particles now uses the high–order WENO scheme proposed by Edwards and Bridson (2012). More importantly, a strong two–way fluid–solid coupling scheme is proposed that can be used within the full particle PIC framework. This coupling scheme combines the approach of cut cell type solid boundaries detailed in Ng et al. (2009) with ideas from the strong fluid–solid coupling technique proposed in Batty et al. (2007). The key point of this coupling methodology is that the velocity of the rigid body has been implicitly represented by the pressure in cells immediately surrounding the solid and integrated into the procedure for solving a suitably amended pressure Poisson equation. This makes the proposed scheme relatively stable and thus able to handle violent interactions between waves and floating structures. We note this scheme should also be straightforward to implement within other projection based incompressible flow solvers. Moreover,

there is nothing to stop the approach being extended to three spatial dimensions. Three test cases including waves impacting a fixed cylinder, roll motion of a rectangular floating box under regular wave action and a floating structure under extreme wave conditions are presented to validate the newly modified PICIN model. The agreement of our results with those from either other numerical methods or experiments is good, showing the capability and potential of the modified PICIN model to simulate surface–piercing floating bodies under differing wave conditions.

Acknowledgements

We thank the reviewers for their constructive comments and suggestions on improving the quality of this paper. The financial support of the University of Bath (Graduate school funding, sponsor code: 3451) and HR Wallingford (internal research project: DDY0485) for this work is greatly appreciated. All authors would like to thank Dr. Giovanni Cuomo, Research Director, HR Wallingford for his continuous support during this project. The first author gratefully thanks both institutions for sponsoring his PhD study. The fourth author acknowledges the support of Prof. Richard Olson, Director of Extreme Events Research at Florida International University. All authors are grateful to Dr. Xizeng Zhao, Associate Professor at Zhejiang University, China, for his kindness in sharing the experimental and numerical data for the third test case. We also thank Dr. Lifen Chen and Dr. Liang Sun of University of Bath for their help on the discussions of FFT analysis in the third test case.

References

Ando, R., Thurey, N., Tsuruno, R., Aug 2012. Preserving fluid sheets with adaptively sampled anisotropic particles. Visualization and Computer Graphics, IEEE Transactions on 18 (8), 1202–1214.

Batty, C., Bertails, F., Bridson, R., 2007. A fast variational framework for accurate solid–fluid coupling. ACM Transactions on Graphics (TOG) 26 (3), 100.

Bhattacharyya, R., 1978. Dynamics of marine vehicles. John Wiley & Sons Inc.

Borazjani, I., Ge, L., Sotiropoulos, F., 2008. Curvilinear immersed boundary method for simulating fluid structure interaction with complex 3D rigid bodies. Journal of Computational Physics 227 (16), 7587 – 7620.
URL http://www.sciencedirect.com/science/article/pii/S0021999108002490

Bouscasse, B., Colagrossi, A., Marrone, S., Antuono, M., 2013. Nonlinear water wave interaction with floating bodies in SPH. Journal of Fluids and Structures 42, 112–129.

Brackbill, J. U., Ruppel, H. M., 1986. FLIP: A method for adaptively zoned, Particle-In-Cell caluclations of fluid flows in two dimensions. J. Comp. Phys. 65, 314–343.

Chen, L., Sun, L., Zang, J., Hillis, A. J., 2014a. Numerical simulation of wave–induced roll of a 2–D rectangular barge using OpenFOAM. In: the 29th International Workshop on Water Waves and Floating Bodies. Osaka, Japan.

Chen, L., Zang, J., Hillis, A. J., Morgan, G. C. J., Plummer, A. R., 2014b. Numerical investigation of wave–structure interaction using OpenFOAM. Ocean Engineering 88, 91–109.

Chen, Q., Kelly, D. M., Dimakopoulos, A. S., Zang, J., Unpublished results. Validation of the PICIN solver for 2D coastal flows. Under Consideration for publication in the Journal of Coastal Engineering.

Chorin, A. J., 1968. Numerical solution of the Navier–Stokes equations. Math. Comput. 22, 745–762.

Dean, R. G., Dalrymple, R. A., 1991. Water wave mechanics for engineers and scientists. Prentice-Hall.

Dixon, A. G., Salter, S. H., Greated, C. A., 1979. Wave forces on partially submerged cylinders. Journal of the Waterway Port Coastal and Ocean Division 105 (4), 421–438.

Downie, M. J., Bearman, P. W., Graham, J. M. R., 4 1988. Effect of vortex shedding on the coupled roll response of bodies in waves. Journal of Fluid Mechanics 189, 243–261.
URL http://journals.cambridge.org/article_S0022112088000990

Edwards, E., Bridson, R., 2012. A high-order accurate Particle–In–Cell method. International Journal for Numerical Methods in Engineering 90 (9), 1073–1088.
URL http://dx.doi.org/10.1002/nme.3356

Faltinsen, O. M., Landrini, M., Greco, M., 2004. Slamming in marine applications. Journal of Engineering Mathematics 48, 187–217.

Fedkiw, R. P., 2002. Coupling an Eulerian fluid calculation to a Lagrangian solid calculation with the ghost fluid method. Journal of Computational Physics 175 (1), 200–224.

Gao, F., Zang, J., 2014. Numerical simulations of breaking waves at vertical wall. In: The Eleventh ISOPE Pacific/Asia Offshore Mechanics Symposium. International Society of Offshore and Polar Engineers.

Ghasemi, A., Pathak, A., Raessi, M., 2014. Computational simulation of the interactions between moving rigid bodies and incompressible two–fluid flows. Computers & Fluids 94, 1 – 13.
URL http://www.sciencedirect.com/science/article/pii/S0045793014000346

Gibou, F., Fedkiw, R. P., Cheng, L.-T., Kang, M., 2002. A second-order-accurate symmetric discretization of the poisson equation on irregular domains. Journal of Computational Physics 176 (1), 205 – 227.
URL http://www.sciencedirect.com/science/article/pii/S0021999101969773

Glowinski, R., Pan, T.-W., Hesla, T. I., Joseph, D. D., 1999. A distributed lagrange multiplier/fictitious domain method for particulate flows. International Journal of Multiphase Flow 25 (5), 755–794.

Goda, Y., 1999. A comparative review on the functional forms of directional wave spectrum. Coastal Engineering Journal 41 (01), 1–20.

Hadžić, I., Hennig, J., Perić, M., Xing-Kaeding, Y., 2005. Computation of flow-induced motion of floating bodies. Applied mathematical modelling 29 (12), 1196–1210.

Harlow, F. H., 1964. The Particle–In–Cell computing method for fluid dynamics. In: Alder, B. (Ed.), Methods in Computational Physics. Academic Press, New York, pp. 319–343.

Harlow, F. H., Welch, J. E., 1965. Numerical calculation of time–dependent viscous incompressible flow of fluid with free surface. Physics of Fluids 8, 2182–2189.

Jacobsen, N. G., Fuhrman, D. R., Fredse, J., 2012. A wave generation toolbox for the open-source CFD library: OpenFoam®. International Journal for Numerical Methods in Fluids 70 (9), 1073–1088.
URL http://dx.doi.org/10.1002/fld.2726

Jung, K. H., 2005. Experimental study on rectangular barge in beam sea. Ph.D. thesis, Texas A&M University.

Jung, K. H., Chang, K.-A., Jo, H. J., 2006. Viscous effect on the roll motion of a rectangular structure. Journal of engineering mechanics 132 (2), 190–200.

Kelly, D. M., 2012. Full particle PIC modelling of the surf and swash zones. In: Proc. 33rd Int. Conf. Coast. Eng. A.S.C.E., Santander, pp. 77–92.
URL http://dx.doi.org/10.9753/icce.v33.currents.30

Kelly, D. M., Chen, Q., Zang, J., 2015. PICIN: A Particle–In–Cell solver for incompressible free surface flows with two-way fluid-solid coupling. SIAM Journal on Scientific Computing 37 (3), B403–B424.
URL http://dx.doi.org/10.1137/140976911

Koo, W., Kim, M.-H., 2004. Freely floating–body simulation by a 2D fully nonlinear numerical wave tank. Ocean Engineering 31 (16), 2011–2046.

Lind, S. J., Stansby, P. K., Rogers, B. D., Lloyd, P. M., 2015. Numerical predictions of water–air wave slam using incompressible–compressible smoothed particle hydrodynamics. Applied Ocean Research 49, 57–71.
URL http://www.sciencedirect.com/science/article/pii/S0141118714001126

Monaghan, J. J., Lattanzio, J. C., 1985. A refined particle method for astrophysical problems. Astronomy and astrophysics 149, 135–143.

Nematbakhsh, A., Olinger, D. J., Tryggvason, G., 2013. A nonlinear computational model of floating wind turbines. Journal of Fluids Engineering 135 (12), 121103.

Ng, Y. T., Min, C., Gibou, F., 2009. An efficient fluid–solid coupling algorithm for single–phase flows. Journal of Computational Physics 228 (23), 8807–8829.

Noh, W. F., 1963. CEL: A time-dependent, two–space–dimensional, coupled eulerian-lagrange code. Tech. rep., Lawrence Radiation Lab., Univ. of California, Livermore.

Oliveira, T. C. A., Sánchez-Arcilla, A., Gironella, X., 2012. Simulation of wave overtopping of maritime structures in a numerical wave flume. Journal of Applied Mathematics 2012.

Patankar, N. A., 2001. A formulation for fast computations of rigid particulate flows. Center for Turbulence Research Annual Research Briefs 2001, 185–196.

Patankar, N. A., Singh, P., Joseph, D. D., Glowinski, R., Pan, T.-W., 2000. A new formulation of the distributed Lagrange multiplier/ fictitious domain method for particulate flows. Int. J. Multiphase Flow 26, 1509–1524.

Peskin, C. S., 1972. Flow patterns around heart valves: a numerical method. Journal of computational physics 10 (2), 252–271.

Peskin, C. S., 2002. The immersed boundary method. Acta numerica 11, 479–517.

Press, W., Flannery, B., Teukolsky, S., Vetterling, W., 1992. Numerical Recipes: The Art of Scientific Computing (second edition). Cambridge Univ. Press, New York.

Purvis, J. W., Burkhalter, J. E., 1979. Prediction of critical Mach number for store configurations. AIAA J. 17, 1170–1177.

Qian, L., Causon, D. M., Mingham, C. G., Ingram, D. M., 2006. A free-surface capturing method for two fluid flows with moving bodies. Proceedings of the Royal Society A: Mathematical, Physical and Engineering Science 462 (2065), 21–42.

Quirk, J. J., 1994. An alternative to unstructured grids for computing gas dynamic flows around arbitrarily complex

two-dimensional bodies. Computers & Fluids 23 (1), 125–142.

Ralston, A., 1962. Runge–Kutta methods with minimum error bound. Mathematics of Computation 16:80, 431–437.

Skillen, A., Lind, S., Stansby, P. K., Rogers, B. D., 2013. Incompressible smoothed particle hydrodynamics (SPH) with reduced temporal noise and generalised Fickian smoothing applied to body–water slam and efficient wave–body interaction. Computer Methods in Applied Mechanics and Engineering 265, 163 – 173.
URL http://www.sciencedirect.com/science/article/pii/S0045782513001448

Weller, S. D., Stallard, T. J., Stansby, P. K., 2013. Experimental measurements of the complex motion of a suspended axisymmetric floating body in regular and near–focused waves. Applied Ocean Research 39, 137–145.

Westphalen, J., Greaves, D. M., Raby, A., Hu, Z. Z., Causon, D. M., Mingham, C. G., Omidvar, P., Stansby, P. K., Rogers, B. D., 2014. Investigation of wave-structure interaction using state of the art CFD techniques. Open Journal of Fluid Dynamics 4, 18–43.

Wilcox, D. C., et al., 1998. Turbulence modeling for CFD. Vol. 2. DCW industries La Canada, CA.

Yang, G., Causon, D. M., Ingram, D. M., 2000. Calculation of compressible flows about complex moving geometries using a three-dimensional cartesian cut cell method. International Journal for Numerical Methods in Fluids 33 (8), 1121–1151.

Ye, T., Mittal, R., Udaykumar, H., Shyy, W., 1999. An accurate cartesian grid method for viscous incompressible flows with complex immersed boundaries. Journal of Computational Physics 156 (2), 209–240.

Zhao, H., 2004. A fast sweeping method for Eikonal equations. Mathematics of Computation 74, 603–627.

Zhao, X., Hu, C., 2012. Numerical and experimental study on a 2-D floating body under extreme wave conditions. Applied Ocean Research 35, 1–13.

Zhao, X., Ye, Z., Fu, Y., Cao, F., 2014. A CIP-based numerical simulation of freak wave impact on a floating body. Ocean Engineering 87, 50–63.

Zhu, Y., Bridson, R., Jul. 2005. Animating sand as a fluid. ACM Trans. Graph. 24 (3), 965–972.
URL http://doi.acm.org/10.1145/1073204.1073298